

# Incorporation of well-dispersed sub-5-nm graphitic pencil nanodots into ordered mesoporous frameworks

Biao Kong<sup>1,2</sup>, Jing Tang<sup>1</sup>, Yueyu Zhang<sup>3</sup>, Tao Jiang<sup>3</sup>, Xingao Gong<sup>3</sup>, Chengxin Peng<sup>4</sup>, Jing Wei<sup>1</sup>, Jianping Yang<sup>1</sup>, Yongcheng Wang<sup>1</sup>, Xianbiao Wang<sup>2</sup>, Gengfeng Zheng<sup>1\*</sup>, Cordelia Selomulya<sup>2\*</sup> and Dongyuan Zhao<sup>1,2\*</sup>

Over the past few decades the direct assembly of optical nanomaterials into ordered mesoporous frameworks has proved to be a considerable challenge. Here we propose the incorporation of ultrasmall (sub-5-nm) graphitic pencil nanodots into ordered mesoporous frameworks for the fabrication of optoelectronic materials. The nanodots, which were prepared from typical commercial graphite pencils by an electrochemical tailoring process, combine properties such as uniform size ( $\sim 3$  nm), excellent dispersibility and high photoconversion efficiency ( $\sim 27\%$ ). These nanodots were incorporated into a variety of ordered mesoporous frameworks ( $\text{TiO}_2$ , silica, carbon and silica-carbon materials) by co-assembly, driven by hydrogen bonding, with the frameworks' precursors. The resulting materials showed a high degree of ordering, and a sharp increase in their optical performance (for example, photocurrent density). We envisage that the large-scale synthesis of ultrasmall carbon nanodots and their incorporation into ordered mesoporous frameworks may facilitate the preparation of materials with a variety of optical properties.

In recent decades mesoporous materials have garnered significant attention<sup>1–3</sup> because of their broad applications in batteries<sup>4,5</sup>, optoelectronics<sup>6</sup>, nanofluidic device<sup>7,8</sup>, sensors<sup>9,10</sup>, photovoltaics<sup>9,11</sup>, ion exchange<sup>12,13</sup>, drug delivery<sup>14,15</sup> and catalysis<sup>16–18</sup>. Among these, the optoelectronic mesoporous materials take advantage of both the optical properties of the guest species and the high surface area of the host mesoporous materials, which leads to tunable optoelectronic platforms<sup>19</sup>. An appropriate introduction of guest species that feature optical properties would maintain the original ordered host mesostructures and so present a promising way to create well-defined functional mesoporous materials<sup>20,21</sup>. At present, a number of ionic, organic and metal-complex-bridged photoactive molecules<sup>12</sup> have been integrated into ordered mesoporous frameworks to pursue these aims. For example, Inagaki *et al.* developed a mesoporous framework doped with coumarin 1 dye for an efficient energy transfer by a dip-coating strategy<sup>22</sup>. Mou and co-workers introduced dual fluorescent dyes into mesoporous silica for pH sensors by a co-condensation method<sup>23</sup>. In addition, Lu and co-workers successfully synthesized various molecule-functionalized mesoporous silica by a vesicle and liquid crystal ‘dual templating’ technique<sup>21</sup>. The incorporation of molecule-modified nanocrystalline silicon in mesoporous organosilica was realized recently through a template-directed self-assembly<sup>24</sup>.

However, the direct *in situ* co-assembly of optical materials, rather than of molecules, into ordered mesoporous frameworks has seldom been reported, mainly for two reasons. First, the self-assembly of mesostructures is driven by weak non-covalent bonds (such as hydrogen bonds, van der Waals forces and electrovalent

bonds) and is susceptible to potential changes of the assembly conditions<sup>25</sup>, which largely limits the possibility of the *in situ* synthesis of optical guest materials during the mesostructure formation. Second, the size effect of incorporating exogenous materials (typically  $>10$  nm) on the co-assembly of inorganic precursors influences the hydrolysis and condensation of the precursors<sup>26,27</sup>. Coupled with the weak driving force for a mesostructure assembly, this eventually leads to a low degree of ordering<sup>28</sup>. To achieve ordered optoelectronic mesostructures, it is necessary to introduce rationally designed guest materials with small sizes that are readily dispersed in common solvents without further surface hydrophilic/hydrophobic modification, and that have a facile interaction with surfactant molecules (for example, amphiphilic block copolymers) via non-covalent-bonding properties.

Here we report a co-assembly strategy to obtain ordered mesoporous optoelectronic materials by the direct incorporation of ultrasmall (sub-5-nm) graphitic pencil nanodots (PNDs) (Fig. 1). The ultrasmall PND, a carbon nanodot generated from the graphite core of a conventional pencil, is composed of only hundreds to thousands of carbon atoms and shows distinctive photophysical and chemical properties, such as resistance to photobleaching, low-toxicity, excellent dispersibility and good stability<sup>29</sup>. The ultrasmall PNDs are synthesized by an electrochemical method and subsequent *in situ* doping of various non-metal atoms. They possess several features that differ from those of conventional carbon nanodots, including naturally high porosities, facile and scalable preparation, abundant hydrogen-bonding sites and facile doping capability (Fig. 1a). We prepared a variety of ordered mesoporous

<sup>1</sup>Collaborative Innovation Center of Chemistry for Energy Materials (iChEM), Department of Chemistry, Laboratory of Advanced Materials, Shanghai Key Laboratory of Molecular Catalysis and Innovative Materials, Fudan University, Shanghai 200433, China. <sup>2</sup>Department of Chemical Engineering, Monash University, Clayton, Victoria 3800, Australia. <sup>3</sup>Key Laboratory of Computational Physical Sciences, Ministry of Education, State Key Laboratory of Surface Physics, Department of Physics, Fudan University, Shanghai 200433, China, and Collaborative Innovation Center of Advanced Microstructures, Nanjing 210093, China. <sup>4</sup>Graphene Research Centre, National University of Singapore, 6 Science Drive 2, Singapore 117546, Singapore. \*e-mail: dyzhao@fudan.edu.cn; gfzheng@fudan.edu.cn; cordelia.selomulya@monash.edu

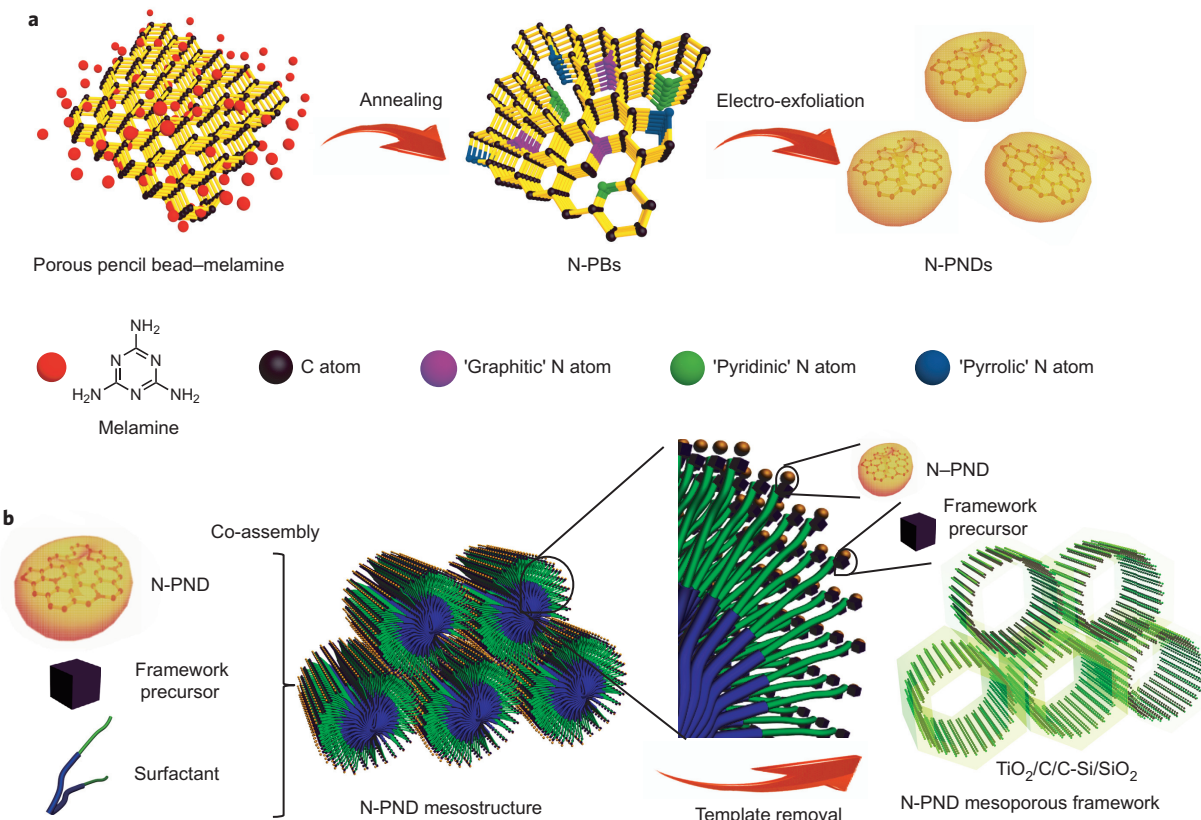


**Figure 1 | Proposed synthesis process and model of the co-assembly.** **a**, Graphitic N-PNDs from *in situ* annealing and electro-exfoliation of pencil beads. N-doped porous pencil beads were first obtained by adsorption of melamine molecules and *in situ* annealing, and the graphitic N-PNDs were then prepared by a process of electro-exfoliation. **b**, The N-PND mesostructures were first obtained via co-assembly of ultrasmall nanodots, precursors of mesoporous materials and surfactants that serve as the template. After template removal, a series of N-PND mesoporous frameworks (which can be TiO<sub>2</sub>, C, C-Si or SiO<sub>2</sub>) is obtained.

frameworks (including mesoporous silica, carbon and TiO<sub>2</sub>) in which ultrasmall graphitic nitrogen-doped pencil nanodots (N-PNDs)—as an example of guest nanodots—were incorporated directly during the co-assembly process. The resulting materials were characterized by extended X-ray absorption fine structure, high-resolution transmission electron microscopy (HRTEM) and optical spectra. The resulting nanodot-inserted materials possess a high degree of ordering, and we envisage that they will show interesting photoelectrochemical properties (Fig. 1b)<sup>30</sup>. This facile and robust approach reduces the effects of the typical hydrolysis and condensation steps on the inorganic species required during the synthesis, and instead co-assembles a variety of species of very diverse sizes: framework precursors, nanodot guests and surfactants that form the framework templates. Compared with its pristine counterpart, the nanodot-doped mesoporous TiO<sub>2</sub> framework showed a sharp increase in its photocurrent density, by approximately 183%. We envision that, by using the proposed incorporation method, various ordered mesoporous materials that encapsulate ultrasmall graphitic PNDs may serve for applications such as photodetectors, photovoltaic solar cells, photodiodes and photoelectrochemical sensors.

## Results

**Fabrication of ultrasmall graphitic PNDs.** Pencil beads were prepared from a commercial pencil via a mechanical exfoliation (Supplementary Fig. 1a). The N-doped pencil beads (N-PBs) were obtained by the pre-absorption of a nitrogen-rich compound, melamine (C<sub>3</sub>H<sub>6</sub>N<sub>6</sub>), on the pencil beads, followed by thermal annealing. Scanning electron microscopy (SEM) images (Supplementary Fig. 2a–c) reveal naturally stacked holes in the raw pencil beads, which are attributed to the stacking of the

nanoscale graphite sheets. The high porosity of the N-PBs obtained, which arises from this natural stacking, can be observed from SEM images (Supplementary Fig. 2d–f), transmission electron microscopy (TEM) images (Supplementary Fig. 2g–i) and nitrogen sorption isotherms (Supplementary Fig. 2j,k). After thermal annealing (Supplementary Fig. 1b), the relatively stable carbon and nitrogen components were retained, as confirmed by X-ray photoelectron spectra (XPS) spectra (Supplementary Fig. 3).

Subsequently, N-doped graphitic PNDs were produced using an electrochemical tailoring method in which the N-PBs serve as both the anode and cathode of an electrochemical device, with NaOH/ethanol as the electrolyte (Supplementary Fig. 4). TEM images (Fig. 2a) show that the exfoliated N-PNDs obtained from the electrochemical tailoring method were uniform (~3 nm) and monodispersed. HRTEM images (Fig. 2b) of a typical N-PND clearly reveal a thickness of a few graphene layers (about ten layers) and a lattice spacing of around 0.32 nm, which agrees well with the (002) spacing of graphitic carbon<sup>31</sup>. Ultraviolet–visible spectra show an enhanced absorption band centred at ~360 nm with N doping (Supplementary Fig. 5a). With an increase in the concentration of the nitrogen doping, the PNDs also show an increase in the absorption coefficient, accompanied by changes in the highest occupied molecular orbital (HOMO) and lowest unoccupied molecular orbital (LUMO) states (Supplementary Figs 5b,c and 6).

Photoluminescence spectra (Fig. 2c) of the N-PNDs displayed under different excitation wavelengths, from 365 to 605 nm, show tunable optical properties. Different emission colours were found in the same sample of N-PND powder under ultraviolet and visible light of wavelengths 365, 405 and 525 nm (Fig. 2d,e). The fluorescence quantum yields of the N-PNDs and undoped PNDs were

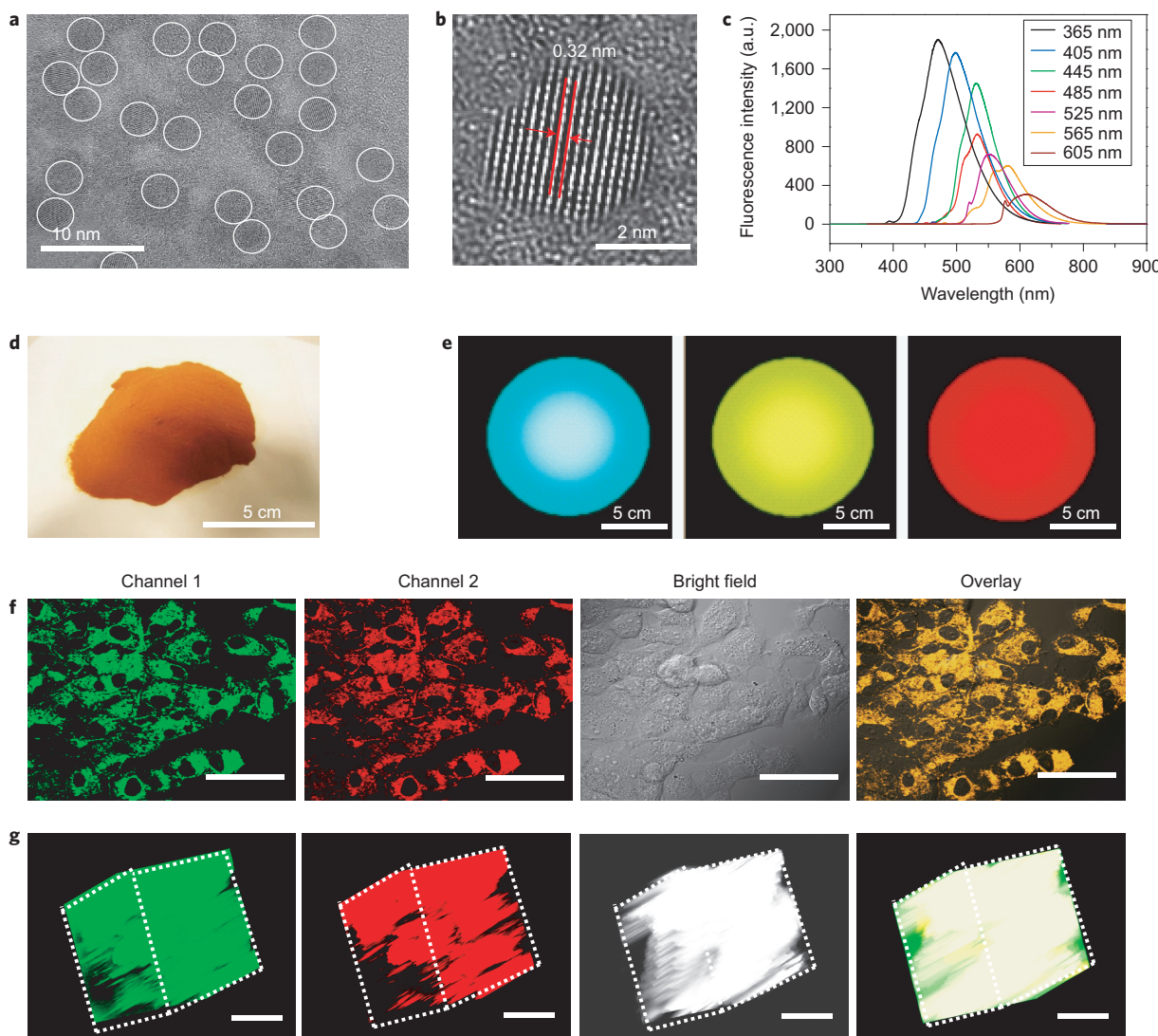


**Figure 2 | Structural analysis and optical properties.** **a**, TEM image of N-PNDs. **b**, HRTEM of a typical N-PND that shows a lattice spacing of 0.32 nm. **c**, Photoluminescence spectra of N-PNDs under different excitation wavelengths from 365 to 605 nm. **d**, Photograph of the N-PNDs prepared on a large (gram) scale. **e**, Typical optical images of a sample of N-PNDs illuminated under ultraviolet and visible light of 365 nm (left), 405 nm (middle) and 525 nm (right). **f,g**, Single-photon confocal microscopy images with different signal channels in HeLa cells (**f**) and mouse LLC-MK2 tissues (**g**) treated with N-PNDs for 24 hours. Different imaging channels are displayed horizontally for each sample (from left to right): green channel (475–525 nm), red channel (575–625 nm), bright field and overlay images. Scale bars, 50  $\mu$ m. a.u., arbitrary units.

~27 and 8%, respectively. The N-PNDs showed photostability for over 12 months (Supplementary Fig. 7). The relationship between the HOMO-LUMO energy gap and quantum-size effect indicates that the photoluminescence generated from the graphitic PNDs can be ascribed to the different sizes (~0.5 to 5.3 nm) of the graphite-fragment structures (Supplementary Fig. 8).

To probe possible future applications in the biomedical domain, we investigated the cell permeability of the nanodots. HeLa cells and tissues of mice (with a thickness of 150  $\mu$ m) were treated with N-PNDs for 24 hours. Single-photon confocal microscopy images with distinct wavelength channels (Fig. 2f,g) of the resulting materials show clear fluorescence signals, which indicates a very good cell permeability and light penetration. The photostability data (Supplementary Fig. 9) of the as-synthesized N-PNDs indicate a promising photostability under two-photon light illumination (from 810 to 910 nm, ~0.50 mW  $\text{cm}^{-2}$  power density). The XPS spectra (Supplementary Fig. 10a,c–e) show that the O/C atomic ratio for the N-PNDs was ~13%, slightly lower than that of the undoped PNDs (~17%). Furthermore, the XPS spectra

(Supplementary Fig. 10b) of a series of N-PNDs obtained under the same synthesis conditions indicate an excellent consistency and controllability of the C/O ratio in the samples. The bands in the infrared spectrum (Supplementary Fig. 10g) located at 3,485, 1,715 and 1,603  $\text{cm}^{-1}$  are ascribed to the stretching vibrations of the O-H, C=O and C-O groups, respectively<sup>31</sup>. Moreover, a control experiment using a hydrogen-plasma treatment to remove the surface oxygen groups suggest that the strong emission mainly comes from the quantum-sized graphite fragment of PNDs (Supplementary Fig. 10f–h). All these data further confirm the presence of –COOH and/or –OH groups at the surface of the nanodots, which are beneficial for further co-assembly driven by hydrogen bonds<sup>25,28</sup>.

**Co-assembly using ultrasmall graphitic PNDs.** Mesoporous N-PND-inserted  $\text{TiO}_2$  frameworks (incorporation ratio (C/Ti atom ratio), ~3.5%) were synthesized by using the diblock copolymer poly(ethylene oxide)-b-polystyrene (PEO-*b*-PS) as the template for the framework pores (Fig. 3a, top). During the process of co-assembly, a titanium compound ( $\text{Ti}(\text{AcAc})_3$ ),

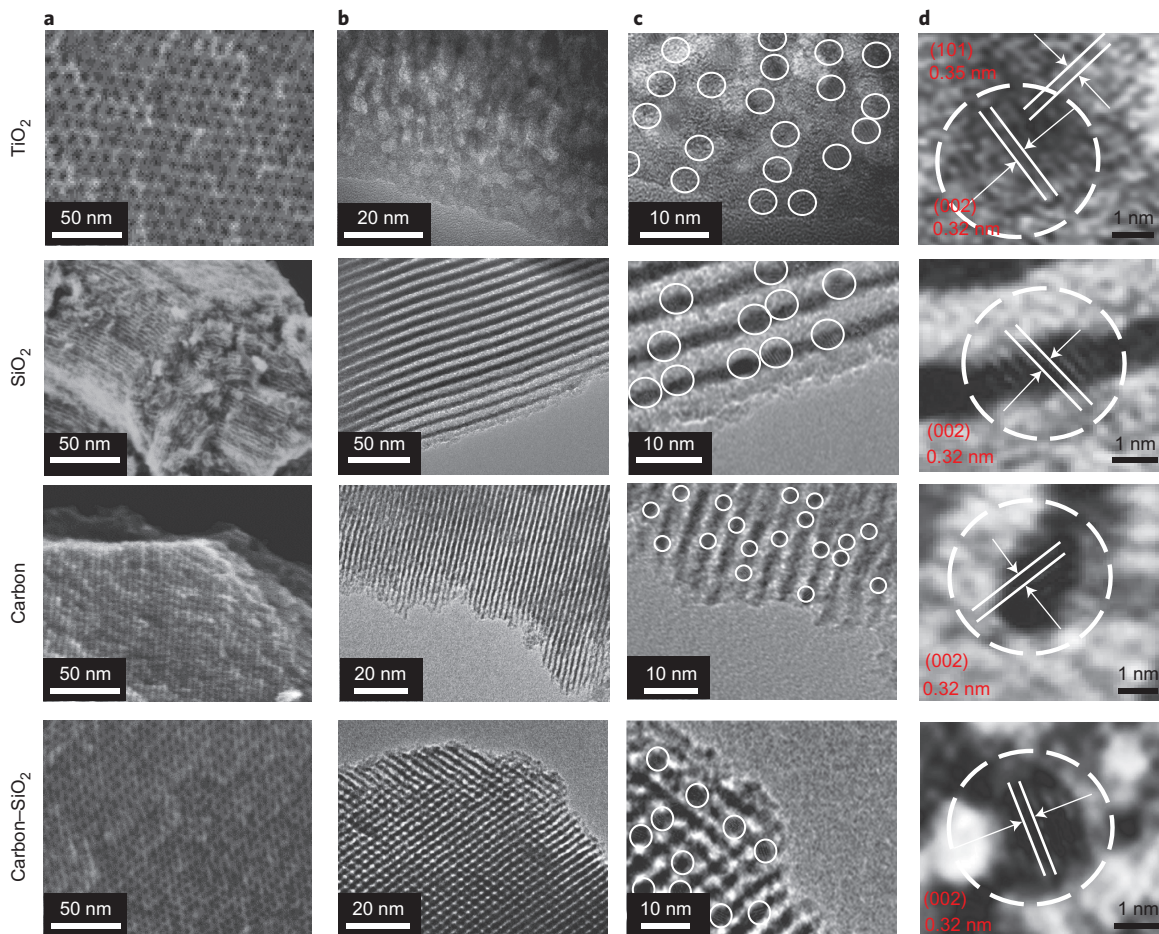


**Figure 3 | The versatile self-inserted co-assembly of the ordered mesoporous structures with ultrasmall nanodots.** **a-d**, SEM images (**a**), TEM images (**b**) and HRTEM images (**c,d**) of the ultrasmall graphitic PND-inserted mesostructures. The PND-inserted mesoporous  $\text{TiO}_2$  obtained by using diblock copolymer PEO-*b*-PS as the template (first row), PND-inserted mesoporous silica using triblock copolymer Pluronic P123 as the template (second row) PND-inserted mesoporous carbon obtained using triblock copolymer F127 as the template (third row) and PND-inserted mesoporous carbon–silica composites prepared by using triblock copolymer F127 as the template (fourth row) via the self-inserted co-assembly method by using ultrasmall graphitic PNDs.

ultrasmall N-PND and  $\text{PEO}_{125}$ -*b*- $\text{PS}_{120}$  served as the precursor, exogenous functional site and template, respectively. The surfaces of N-PND, which feature  $-\text{COOH}$  and/or  $-\text{OH}$  groups, are suited to co-assembly driven by hydrogen bonds and further enable the formation of ordered mesostructures from the N-PNDs and structure-directing agents of the  $\text{TiO}_2$  framework (Supplementary Methods). The TEM (Fig. 3b, top) and HRTEM (Fig. 3c, top) images of the material that result from the co-assembly of the N-PNDs and framework precursors show a well-ordered mesostructure, inserted with ultrasmall ( $\sim 3$  nm) N-PNDs. The HRTEM image (Fig. 3d, top) of a typical N-PND in mesopore walls presents single-crystalline and well-resolved lattice fringes (with a  $d$  spacing of 0.32 nm), which correspond to the (002) plane of graphitic carbon and suggests the successful incorporation into the mesostructure<sup>31</sup>. The small-angle X-ray scattering (SAXS) pattern (Supplementary Fig. 11a) reveals poorly resolved scattering peaks associated with three-dimensional (3D) body-centred symmetry (space group  $\text{Im}3\text{m}$ )<sup>32</sup>. Nitrogen sorption isotherms (Supplementary Fig. 12a) exhibit a type-IV curve with a  $\text{H}_2$ -type hysteresis loop and distinct condensation steps<sup>17</sup>. The surface area of the obtained N-PND-inserted mesoporous  $\text{TiO}_2$  was  $\sim 97 \text{ m}^2 \text{ g}^{-1}$ , and the mean pore-size distribution was centred at  $\sim 13.5$  nm.

Other mesoporous frameworks (silica, carbon and carbon–silica composites) were also obtained through the same co-assembly strategy. The SAXS pattern of the N-PND-inserted mesoporous silica

(Supplementary Fig. 11b) obtained by using the triblock copolymer Pluronic P123 as the template reveals three diffraction peaks (the 100, 110 and 200 reflections) of 2D hexagonal mesostructure (space group  $p6mm$ )<sup>33</sup>. The SAXS pattern of the N-PND-inserted mesoporous carbon (Supplementary Fig. 11c) prepared using the triblock copolymer F127 as the template shows three scattering peaks (the 10, 11 and 20 reflections) of an ordered 2D hexagonal mesostructure (space group  $p6mm$ )<sup>34</sup>. The SAXS pattern of the N-PND-inserted mesoporous carbon–silica composites (Supplementary Fig. 11d) prepared using F127 as the template reveals three scattering peaks, well indexed to the 10, 11 and 20 reflections of an ordered 2D hexagonal mesostructure (space group  $p6mm$ ). Nitrogen sorption isotherms (Supplementary Fig. 12c,e,g) of the N-PND-inserted mesoporous materials (silica, carbon and carbon–silica) exhibit type-IV curves with  $\text{H}_2$ -type hysteresis loops and distinct condensation steps. The surface areas were calculated to be  $\sim 651$ , 396 and  $486 \text{ m}^2 \text{ g}^{-1}$  for the N-PND-inserted mesoporous silica, carbon and carbon–silica composite, respectively. The pore-size-distribution curves (Supplementary Fig. 12d,f,h) show that the N-PND-inserted mesoporous materials had uniform pore diameters of about 8.2, 5.5 and 5.6 nm, respectively (Supplementary Table 1). No obvious pore blockage was found from the nitrogen sorption isotherms and pore-size-distribution curves, measured with and without N-PND insertion (Supplementary Fig. 13 and Supplementary Table 2).

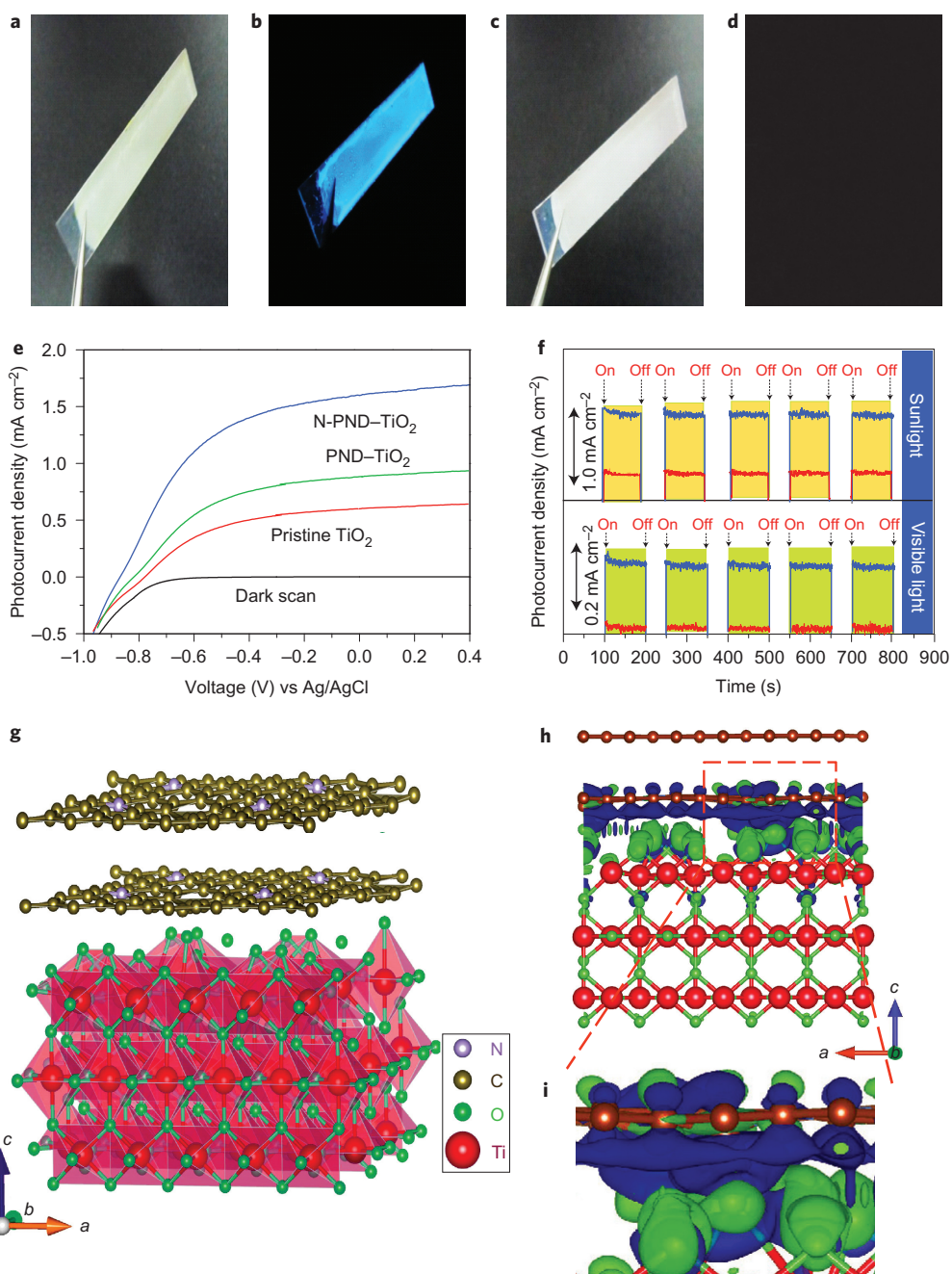


**Figure 4 | Optoelectronic performance.** **a,b**, Photographs of the N-PND-TiO<sub>2</sub> under visible light (**a**) and ultraviolet light (**b**). **c,d**, Photographs of the pristine mesoporous TiO<sub>2</sub> under visible light (**c**) and ultraviolet light (**d**). **e**, Photocurrent densities versus voltage measured from the pristine mesoporous TiO<sub>2</sub>, PND-inserted mesoporous TiO<sub>2</sub> and N-PND-TiO<sub>2</sub>. **f**, Amperometric *I-t* curves for N-PND-TiO<sub>2</sub> and pristine mesoporous TiO<sub>2</sub> under simulated sunlight (top) and visible-light (bottom) illumination. **g**, Structure model for a computational simulation of the interface of N-PNDs (top) and the (110) surface of TiO<sub>2</sub> (bottom). **h,i**, 3D charge-density difference for the interface of N-PNDs and TiO<sub>2</sub> (110) with an isovalue of 0.003 e Å<sup>-3</sup>. Green and blue isosurfaces represent charge accumulation and depletion in the space.

**Photoelectrochemical properties of PND mesoporous materials.** The N-PND-inserted mesoporous TiO<sub>2</sub> (N-PND-TiO<sub>2</sub>) was then used as a photoanode for optoelectronic studies that employed a transparent three-electrode electrochemical cell, which consisted of a modified N-PND-TiO<sub>2</sub> working electrode, a counter electrode of platinum wire and a KCl-saturated Ag/AgCl electrode under simulated sunlight. Optical photographs (Fig. 4a,b) show that the N-PND-TiO<sub>2</sub> has a blue-green colour emission under ultraviolet light excitation, whereas in a control experiment with the pristine mesoporous TiO<sub>2</sub> no emission was found (Fig. 4c,d). Under a simulated solar-light illumination of air mass 1.5 global

(AM 1.5G), the photocurrent densities of the pristine mesoporous TiO<sub>2</sub> and undoped PND-TiO<sub>2</sub> were measured to be ~0.61 and 0.83 mA cm<sup>-2</sup>, respectively. The N-PND-TiO<sub>2</sub> exhibited a high photocurrent density of ~1.73 mA cm<sup>-2</sup> at 0.23 V versus Ag/AgCl, ~183 and 108% increase of the values found for the pristine mesoporous TiO<sub>2</sub> and undoped PND-TiO<sub>2</sub>, respectively (Fig. 4e). A schematic energy diagram of the mesoporous N-PND-TiO<sub>2</sub> with the visible-light-induced transfer of electrons and holes is shown in Supplementary Fig. 14a. The incident photo-to-current conversion efficiency (IPCE) measurements show that the N-PND-inserted mesoporous TiO<sub>2</sub> had an IPCE value of ~50%

over the wavelength range of 325–425 nm, more than twice that for the pristine mesoporous  $\text{TiO}_2$  (Supplementary Fig. 14b). The slight reduction of fluorescence lifetime confirms the process of photocurrent enhancement via electron injection into the  $\text{TiO}_2$  frameworks (Supplementary Fig. 14b). Moreover, the time-dependent photocurrent measurements of the N-PND-inserted mesoporous  $\text{TiO}_2$  displayed a highly stable and sensitive photocurrent density under on/off cycles of simulated solar illumination without observable degradation (Fig. 4f).

The mechanism with regard to the influence of N-PNDs on  $\text{TiO}_2$  frameworks is illustrated further by density functional theory simulation<sup>35</sup>. To simulate the interface between the N-PNDs and  $\text{TiO}_2$  frameworks, several models of different carbon layers doped by N atoms on  $\text{TiO}_2$  (110) surfaces were used in our calculation (Fig. 4g, and Supplementary Figs 15 and 16). To characterize the change of electronic structure at the interface, 3D plots of charge-density difference were calculated by subtracting the electronic charge of a hybrid carbon– $\text{TiO}_2$  nanocomposite from that of the separate single-layer carbon plus that of  $\text{TiO}_2$  (110) surface (Fig. 4h,i). The enhanced charge transfer may be attributed to the large difference in work functions at the interface of carbon and  $\text{TiO}_2$  (refs 36,37). Therefore, with N-doping, the charge-transfer rate between the PNDs and  $\text{TiO}_2$  frameworks is enhanced dramatically because of the electron donation from the doped N atoms.

**Synthesis of other doped PNDs.** Other non-metallic atom-doped pencil beads, including boron (B)-, phosphorus (P)- and sulfur (S)-doped pencil beads, were obtained by a similar process of the *in situ* pre-adsorption of precursors that contained B, P or S (boron oxide ( $\text{B}_2\text{O}_3$ ), triphenylphosphine ( $(\text{C}_6\text{H}_5)_3\text{P}$ ) and benzyl disulfide ( $\text{C}_6\text{H}_5\text{CH}_2\text{SSCH}_2\text{C}_6\text{H}_5$ ), respectively) in the natural porosity of the pencil beads, followed by thermal annealing (Supplementary Figs 17–19). The SEM images (Supplementary Figs 17a–c, 18a–c and 19a–c) and nitrogen sorption isotherms (Supplementary Figs 17d,e, 18d,e and 19d,e) show that the obtained porosity of the doped pencil beads results from stacked hierarchical pore structures, analogous to the N-PBs. Subsequently, N-, B-, P- and S-doped graphitic PNDs with bright fluorescence emissions and excellent photostability were obtained by a similar approach (Supplementary Figs 20–22). TEM images and HRTEM images (Supplementary Fig. 20) demonstrate that the obtained B-, P-, S-PNDs are monodispersed with narrow size distributions (diameters of  $\sim 3$  nm) and lattice spacing (around 0.32 nm), which correspond to the  $\langle 002 \rangle$  spacing of graphitic carbon. XPS spectra confirm that stable carbon, boron, phosphorus and sulfur are retained during thermal annealing (Supplementary Fig. 20)<sup>38</sup>. The ultrasmall PNDs demonstrated excellent photostability towards different temperatures, pH and small-molecule interferences (Supplementary Figs 23–27). The heteroatom-doped PNDs were obtained from various types of commercial pencils (such as 1B–6B, HB, F and 1H–6H) using an electrochemical tailoring method, with almost identical crystallinity, sizes and morphology, which allowed for a higher charge-carrier mobility and broad-light absorbance compared with those of the pristine PNDs (Supplementary Figs 28 and 29)<sup>39</sup>. Furthermore, the optical properties and appearance of the PNDs remained unchanged after storing for 12 months in air at room temperature.

## Discussion

It is proposed that the doping of pencil beads with non-metallic species (N, B, P and S atoms) occurs by *in situ* pre-adsorption of the heteroatoms and subsequent thermal annealing (Fig. 1a, Supplementary Fig. 30). This heteroatom-doping approach can be broadly applied to a variety of non-metallic dopants by host–guest chemistry between porous pencil beads and guest dopant molecules. Four non-metallic elements (N, B, P and S) with various electron

negativities were selected to obtain single-doped pencil beads. The resulting N-, B-, P- and S-doped pencil beads have consistent porous structures from the hierarchical pore stacking. The physico-chemical properties of the doped pencil beads, such as morphology, surface area and porosity, are well preserved without noticeable residues of the solid precursors in all four of the resultant samples (N-, B-, P- and S-doped pencil beads). Nitrogen sorption isotherms indicate that all the pencil beads have similar surface areas in a range between 40 and  $65 \text{ m}^2 \text{ g}^{-1}$ . Given that the concentrations of all doped heteroatoms are also similar ( $\sim 5$  atom%), it is expected that the difference in the optical activity of various doped PND samples does not originate from their physicochemical properties, but from the nature of the dopant that affects their optical activities.

For the synthesis of graphitic PNDs, a mechanism of electrochemical tailoring (Fig. 1a, Supplementary Fig. 31) from porous heteroatom-doped pencil beads is proposed. These heteroatom-doped pencil beads are designed to serve as both anode and cathode in an electrochemical cell using NaOH/ethanol as the electrolytes. The electrolyte solution changes from colourless to yellow with a current intensity of  $\sim 50 \text{ mA cm}^{-2}$ , which indicates the exfoliation of PNDs from the pencil beads and their accumulation in solution. Control experiments using acids (HCl/ethanol,  $\text{HNO}_3$ /ethanol and  $\text{H}_2\text{SO}_4$ /ethanol) as electrolytes did not yield PNDs. Control experiments using electrolytes without ethanol (NaOH/acetone, NaOH/tetrahydrofuran and NaOH/acetate) also failed to produce PNDs. These results show that both alkali and alkoxide are key factors, and that  $\text{OH}^-$  and  $\text{C}_2\text{H}_5\text{ONa}$  are essential for the formation of PNDs during the electrochemical tailoring process. During this process, the solution colour becomes darker and ultrasmall PNDs are released by oxidation of the pencil bead anode by  $\text{O}^\bullet$  and  $\text{OH}^\bullet$  radicals. The oxidation occurs initially at graphite-edge sites, grain boundaries or defect sites, which results in the opening up of the edge sheets. This opening facilitates the subsequent depolarization and expansion of the graphite anode, and thereby breaks the graphite domains near these defects to release PNDs. The passivated surfaces rich in –COOH and/or –OH groups offer great potential for a further self-inserted co-assembly driven by hydrogen bonds.

As mentioned above, it is proposed that for the formation of ordered mesostructures, the ultrasmall nanodots are incorporated into various mesostructures via a co-assembly step driven by hydrogen bonding (Fig. 1b). The assembly enables the formation of ordered mesostructures with exogenous N-PNDs and structure-directing agents (for example, amphiphilic surfactants of block copolymers). In these processes, the amphiphilic surfactants and/or copolymers co-assemble together with the ultrasmall photoactive graphitic PNDs and the inorganic precursors into ordered mesostructures<sup>25,26</sup>. The organizing ability of the amphiphilic copolymers and the diffusibility of the framework precursors place practical limits on the size of the nanodots and precursors that can be used for a successful co-assembly. Unlike conventional guest molecules or oligomers, the ultrasmall heteroatom-doped PNDs can be dispersed readily in water, tetrahydrofuran and ethanol, and give a transparent appearance to the solution without the need for the addition of cosolvents, surface hydrophilic/hydrophobic modification or ultrasonic dispersion. In the absence of further surface modification and ultrasonic dispersion, the original ultrasmall sizes of nanodots can be maintained for subsequent ordered self-inserted assembly, which overcomes size effects on the co-assembly of inorganic precursors by the incorporation of exogenous materials<sup>28</sup>. Owing to their rich hydrophilic groups, the direct interaction from hydrogen-bond-driven hydrolysis and condensation of the precursors (such as  $\text{TiO}_2$ , silica and carbon) can occur on graphitic PNDs, which can be further assembled into ordered spherical, rod-like and disc-like composite micelles<sup>20</sup>. Furthermore, critical for a successful co-assembly, the ultrasmall sizes of PNDs allow for a

hydrogen-bond-driven direct insertion into the gaps of micelles and mesopore-frameworks, whereas it remains generally challenging to drive the assembly of larger size ( $>5$  nm) exogenous materials with relatively weak non-covalent bonds.

In conclusion, we have demonstrated an effective co-assembly strategy to incorporate ultrasmall graphitic PNDs ( $<5$  nm) within ordered mesostructures by hydrogen bonding. The original ultrasmall sizes of carbon nanodots with rich hydrogen-bonding sites, which are easily prepared from commercial pencil graphite beads by an electrochemical tailing method, overcome the size effects on the co-assembly of inorganic precursors by the incorporation of exogenous materials. This strategy is applicable to a broad range of mesoporous materials, which allows the incorporation of optical guest materials in a well-dispersed fashion, and is capable of controlling the spatial distribution of ultrasmall nanodots within the mesoporous framework matrix. The as-obtained PND mesoporous composites encompass the benefit of porous and molecular-sieving behaviours of the mesoporous matrix, together with the functionality typical of isolated ultrasmall graphitic nanodots. In addition, the assembly of other ultrasmall nanodots, such as semiconductor quantum dots and metal nanoclusters, with high photoelectrochemical efficiencies using this method can be achieved, as long as the controlled growth and surface/interface modification of ultrasmall nanodots are well developed. Our work highlights natural porous pencil beads as a widely available carbon source for the versatile heteroatom-doped functional graphitic PNDs. The capability of incorporating various types of ultrasmall nanodots from this co-assembly approach will also open up many new possibilities for practical applications of nanodot-enabled ordered mesoporous structures.

## Methods

All the technical details, procedures and sequences are provided in the Supplementary Information. Procedures with the cell and animal cultures used in this study were performed in accordance with the Guide of Fudan University for the Care and Use of Laboratory Animals and were approved by the Committee on Animal Care of Fudan University.

Received 2 April 2015; accepted 20 October 2015;  
published online 30 November 2015

## References

- Zhao, D. Y. *et al.* Triblock copolymer syntheses of mesoporous silica with periodic 50 to 300 angstrom pores. *Science* **279**, 548–552 (1998).
- Tian, B. *et al.* Self-adjusted synthesis of ordered stable mesoporous minerals by acid-base pairs. *Nature Mater.* **2**, 159–163 (2003).
- Lee, J. S., Wang, X., Luo, H., Baker, G. A. & Dai, S. Facile ionothermal synthesis of microporous and mesoporous carbons from task specific ionic liquids. *J. Am. Chem. Soc.* **131**, 4596–4597 (2009).
- Liu, J. *et al.* A facile soft-template synthesis of mesoporous polymeric and carbonaceous nanospheres. *Nature Commun.* **4**, 2789 (2013).
- Guo, B. *et al.* Soft-templated mesoporous carbon–carbon nanotube composites for high performance lithium-ion batteries. *Adv. Mater.* **23**, 4661–4666 (2011).
- Baeck, S. H., Choi, K. S., Jaramillo, T. F., Stucky, G. D. & McFarland, E. W. Enhancement of photocatalytic and electrochromic properties of electrochemically fabricated mesoporous  $\text{WO}_3$  thin films. *Adv. Mater.* **15**, 1269–1273 (2003).
- Gao, J. *et al.* High-performance ionic diode membrane for salinity gradient power generation. *J. Am. Chem. Soc.* **136**, 12265–12272 (2014).
- Fan, R., Huh, S., Yan, R., Arnold, J. & Yang, P. Gated proton transport in aligned mesoporous silica films. *Nature Mater.* **7**, 303–307 (2008).
- Li, Y. *et al.* Highly ordered mesoporous tungsten oxides with a large pore size and crystalline framework for  $\text{H}_2\text{S}$  sensing. *Angew. Chem. Int. Ed.* **53**, 9035–9040 (2014).
- Qin, Y. *et al.* Hierarchically porous CuO hollow spheres fabricated via a one-pot template-free method for high-performance gas sensors. *J. Phys. Chem. C* **116**, 11994–12000 (2012).
- Neyshadt, S. *et al.* Understanding and controlling organic–inorganic interfaces in mesostructured hybrid photovoltaic materials. *J. Am. Chem. Soc.* **133**, 10119–10133 (2011).
- Inagaki, S., Guan, S., Ohsuna, T. & Terasaki, O. An ordered mesoporous organosilica hybrid material with a crystal-like wall structure. *Nature* **416**, 304–307 (2002).
- Klaysom, C., Moon, S.-H., Ladewig, B. P., Lu, G. Q. M. & Wang, L. The influence of inorganic filler particle size on composite ion-exchange membranes for desalination. *J. Phys. Chem. C* **115**, 15124–15132 (2011).
- Fang, W., Yang, J., Gong, J. & Zheng, N. Photo- and pH-triggered release of anticancer drugs from mesoporous silica-coated Pd@Ag nanoparticles. *Adv. Funct. Mater.* **22**, 842–848 (2012).
- Yu, A., Wang, Y., Barlow, E. & Caruso, F. Mesoporous silica particles as templates for preparing enzyme-loaded biocompatible microcapsules. *Adv. Mater.* **17**, 1737–1741 (2005).
- Lee, C.-H., Lin, T.-S. & Mou, C.-Y. Mesoporous materials for encapsulating enzymes. *Nano Today* **4**, 165–179 (2009).
- Galeano, C. *et al.* Toward highly stable electrocatalysts via nanoparticle pore confinement. *J. Am. Chem. Soc.* **134**, 20457–20465 (2012).
- Fang, X. *et al.* Hollow mesoporous aluminosilica spheres with perpendicular pore channels as catalytic nanoreactors. *ACS Nano* **6**, 4434–4444 (2012).
- Scott, B. J., Wirnsberger, G. & Stucky, G. D. Mesoporous and mesostructured materials for optical applications. *Chem. Mater.* **13**, 3140–3150 (2001).
- Wan, Y. & Zhao, D. Y. On the controllable soft-templating approach to mesoporous silicates. *Chem. Rev.* **107**, 2821–2860 (2007).
- Qiao, S. Z. *et al.* Surface-functionalized periodic mesoporous organosilica hollow spheres. *J. Phys. Chem. C* **113**, 8673–8682 (2009).
- Inagaki, S. *et al.* Light harvesting by a periodic mesoporous organosilica chromophore. *Angew. Chem. Int. Ed.* **48**, 4042–4046 (2009).
- Tsou, C.-J., Chu, C.-Y., Hung, Y. & Mou, C.-Y. A broad range fluorescent pH sensor based on hollow mesoporous silica nanoparticles, utilising the surface curvature effect. *J. Mater. Chem. B* **1**, 5557–5563 (2013).
- Guan, M. *et al.* Assembling photoluminescent silicon nanocrystals into periodic mesoporous organosilica. *J. Am. Chem. Soc.* **134**, 8439–8446 (2012).
- Wan, Y., Yang, H. & Zhao, D. Y. ‘Host–guest’ chemistry in the synthesis of ordered nonsiliceous mesoporous materials. *Acc. Chem. Res.* **39**, 423–432 (2006).
- Petkovich, N. D. & Stein, A. Controlling macro- and mesostructures with hierarchical porosity through combined hard and soft templating. *Chem. Soc. Rev.* **42**, 3721–3739 (2013).
- Rebbin, V., Rothkirch, A., Ohta, N., Hikima, T. & Funari, S. S. Size limit on the formation of periodic mesoporous organosilicas (PMOs). *Langmuir* **30**, 1900–1905 (2014).
- Wang, Y. & Hu, A. Carbon quantum dots: synthesis, properties and applications. *J. Mater. Chem. C* **2**, 6921–6939 (2014).
- Ding, C., Zhu, A. & Tian, Y. Functional surface engineering of C-dots for fluorescent biosensing and *in vivo* bioimaging. *Acc. Chem. Res.* **47**, 20–30 (2013).
- Zhang, R. *et al.* Ordered macro-/mesoporous anatase films with high thermal stability and crystallinity for photoelectrocatalytic water-splitting. *Adv. Energy Mater.* **4**, 1301725 (2014).
- Kong, B. *et al.* Carbon dot-based inorganic–organic nanosystem for two-photon imaging and biosensing of pH variation in living cells and tissues. *Adv. Mater.* **24**, 5844–5848 (2012).
- Feng, D. *et al.* Multi-layered mesoporous  $\text{TiO}_2$  thin films with large pores and highly crystalline frameworks for efficient photoelectrochemical conversion. *J. Mater. Chem. A* **1**, 1591–1599 (2013).
- Wang, M. *et al.* An interface-directed coassembly approach to synthesize uniform large-pore mesoporous silica spheres. *J. Am. Chem. Soc.* **136**, 1884–1892 (2014).
- Sun, Z. *et al.* A general chelate-assisted co-assembly to metallic nanoparticles—incorporated ordered mesoporous carbon catalysts for Fischer–Tropsch synthesis. *J. Am. Chem. Soc.* **134**, 17653–17660 (2012).
- Blöml, P. Projector augmented-wave method. *Phys. Rev. B* **50**, 17953–17979 (1994).
- Tang, W., Sanville, E. & Henkelman, G. A grid-based Bader analysis algorithm without lattice bias. *J. Phys. Condens. Matter* **21**, 084204 (2009).
- Du, A. *et al.* Hybrid graphene/titania nanocomposite: interface charge transfer, hole doping, and sensitization for visible light response. *J. Phys. Chem. Lett.* **2**, 894–899 (2011).
- Jiao, Y., Zheng, Y., Jaroniec, M. & Qiao, S. Z. Origin of the electrocatalytic oxygen reduction activity of graphene-based catalysts: a roadmap to achieve the best performance. *J. Am. Chem. Soc.* **136**, 4394–4403 (2014).
- Tang, J. *et al.* Solar-driven photoelectrochemical probing of nanodot/nanowire/cell interface. *Nano Lett.* **14**, 2702–2708 (2014).

## Acknowledgements

This work was supported by the State Key Basic Research Program of China (2012CB224805, 2013CB934104), the National Natural Science Foundation of China (21210004, 21322311 and 21473038), the Shanghai Leading Academic Discipline Project (B108), the Science and Technology Commission of Shanghai Municipality (14JC1400700, 14JC1490500), the Australian Research Council (DP120101194, DP140104062) and the Deanship of Scientific Research of King Saud University (IHCRG#14-102, RG#1435-010).

**Author contributions**

B.K., G.Z., C.S. and D.Y.Z. conceived the idea of the project. B.K. devised and performed syntheses and characterization of the materials. B.K., J.T., T.J., C.P., J.W., J.Y., Y.W. and X.W. performed structural characterization, device fabrication, performance measurements and data analysis. Y.Z. and X.G. developed the structural models and carried out the numerical simulations. B.K., C.S., G.Z. and D.Y.Z. wrote the manuscript. All the authors discussed the results and commented on the manuscript at all stages.

**Additional information**

Supplementary information is available in the [online version](#) of the paper. Reprints and permissions information is available online at [www.nature.com/reprints](http://www.nature.com/reprints). Correspondence and requests for materials should be addressed to G.Z., C.S. and D.Z.

**Competing financial interests**

The authors declare no competing financial interests.